Vertical mode expansion method for analyzing elliptic cylindrical objects in a layered background

Hualiang Shi[1] and Ya Yan Lu[1,*]

[1]*Department of Mathematics, City University of Hong Kong, Kowloon, Hong Kong*

compiled: February 25, 2015

The vertical mode expansion method (VMEM) (X. Lu *et al.*, J. Opt. Soc. Am. A **31**, 293-300, 2014) is a frequency-domain numerical method for solving Maxwell's equations in structures that are layered separately in a cylindrical region and its exterior. Based on expanding the electromagnetic field in one-dimensional vertical modes, VMEM reduces the original three-dimensional problem to a two-dimensional (2D) problem on the vertical boundary of the cylindrical region. However, VMEM has so-far only been implemented for structures with circular cylindrical regions. In this paper, we develop a VMEM for structures with an elliptic cylindrical region, based on separation of variables in the elliptic coordinates. A key step in VMEM is to calculate the so-called Dirichlet-to-Neumann (DtN) maps for 2D Helmholtz equations inside or outside the ellipse. For numerical stability reasons, we avoid the analytic solutions of the Helmholtz equations in terms of the angular and radial Mathieu functions, and construct the DtN maps by a fully numerical method. To illustrate the new VMEM, we analyze the transmission of light through an elliptic aperture in a metallic film, and the scattering of light by elliptic gold cylinders on a substrate.

OCIS codes: (000.4430) Numerical approximation and analysis; (050.1755) Computational electromagnetic methods.

http://dx.doi.org/10.1364/XX.99.099999

1. Introduction

In computational electromagnetics, a fundamental problem is to calculate the scattering field of an incident electromagnetic wave by a given scatterer embedded in a layered background. For applications in photonics, the scatterer is often penetrable and has subwavelength features, and it could include highly dispersive components, such as metals. Among the many existing numerical methods for scattering problems, the most popular ones are the finite-difference time-domain method (FDTD) [1] and the frequency-domain finite element method (FEM) [2, 3]. FDTD is relatively simple to implement and extremely versatile, but is often relatively inefficient for modeling plasmonic structures, since very small grid sizes and time steps are needed to capture rapid field changes in metals, and proper dispersion models must be incorperated into the method. FEM is widely used and capable of resolving small features effectively by locally refined meshes, but it gives rise to large linear systems that could be expensive to solve. The boundary integral equation (BIE) method [4, 5] is another important method, but it becomes rather complicated when the scatterer has components with different material properties.

Structures designed for practical applications often have special geometric features. In that case, it is desirable and often possible to develop special numerical or semi-analytic methods that are more efficient than the general methods. The standard mode-matching method (MMM, also called modal method) including its numerical variants [6–12], is useful when the structure is piecewise uniform in one spatial direction. It is based on expanding the electromagnetic field in each uniform layer in transverse eigenmodes. For three-dimensional (3D) structures, MMM is not very efficient, since the eigenmodes are functions of two transverse variables and usually they can only be calculated numerically.

The vertical mode expansion method (VMEM) [13] is a special method for 3D structures consisting of layered media in different regions, i.e., the material properties in each region depend only on one spatial variable (assuming it is the vertical variable z). In each region, VMEM expands the electromagnetic field in one-dimensional (1D) vertical modes where the "expansion coefficients" are functions of the two horizontal variables satisfying two-dimensional (2D) Helmholtz equations. In earlier works [14, 15], VMEM has been used to analyze dielectric slabs with air holes where the incident wave is a propagating mode of the slab. The method has also been used to analyze photonic crystal slab waveguides [16]. In [13], VMEM was formulated for scattering problems with general incident waves, and applied to analyze the transmission of light through a circular aperture in a metallic film. Since only circular holes are involved in these studies [13–16], cylindrical wave ex-

* Corresponding author: mayylu@cityu.edu.hk

pansions are used to represent the solutions of the 2D Helmholtz equations.

In this paper, we consider the scattering of light by a single elliptic cylinder embedded in a (generally) layered background. In particular, we analyze the transmission of light through an elliptic aperture in a metallic film, and the scattering of light by an elliptic cylinder of finite height. The solutions of a 2D Helmholtz equation inside or outside an ellipse can be expanded in angular and radial Mathieu functions [17, 18], but the method based on the analytic expansions appears to be numerically unstable, mainly because the Helmholtz equations in VMEM have complex coefficients. We present a stable method based on a numerical separation of variables in the elliptic coordinates. The method is used to analyze elliptic apertures in a metallic film [19], and to study the scattering of light by gold elliptic cylinders on a substrate. Numerical results indicate that VMEM is capable of delivering accurate solutions with relatively small computing efforts.

2. Vertical mode expansions

In [13], VMEM was developed for the special case where a layered circular cylinder is surrounded by a layered medium, but the main ideas are applicable to the more general case where the cylinder has an arbitrary cross section. In the following, we give a brief summary for the key steps of VMEM.

Consider a structure bounded in the z direction by $0 < z < D$, and surrounded by homogeneous media in the top ($z > D$) and the bottom ($z < 0$), where z is identified as the "vertical" variable, and D is the thickness of the structure. A special case with an elliptic cylindrical object is shown in Fig. 1. In the top and bottom

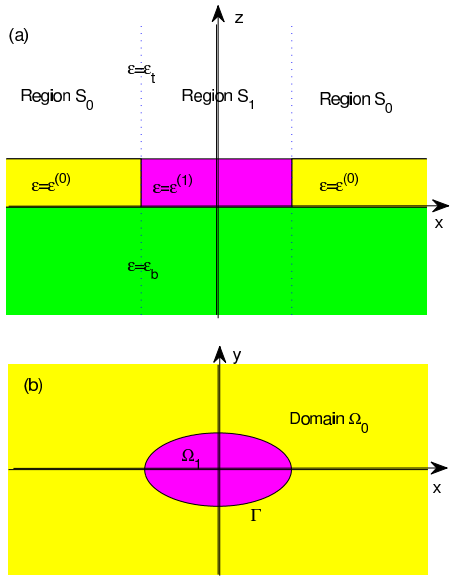

Fig. 1. Elliptic cylindrical object in a layered background: (a) cross section in xz plane, (b) cross section in xy plane.

homogeneous media, we have $\varepsilon = \varepsilon_t$, $\mu = \mu_t$ $(z > D)$ and $\varepsilon = \varepsilon_b$, $\mu = \mu_b$ $(z < 0)$, respectively, where ε is the relative permittivity, μ is the relative permeability, ε_t, μ_t, ε_b and μ_b are real constants. In the horizontal xy plane, we have a bounded domain Ω_1 and its exterior Ω_0, where Ω_1 is the cross section of the cylinder. The entire 3D space is divided into a cylindrical region S_1 and its complement S_0, where

$$S_l = \{(x, y, z) \ : \ (x, y) \in \Omega_l, \ -\infty < z < \infty\}$$

for $l = 0$, 1. In S_0 and S_1, the structure is layered. That is,

$$\varepsilon = \varepsilon^{(l)}(z), \ \mu = \mu^{(l)}(z) \text{ for } (x, y, z) \in S_l. \tag{1}$$

To be consistent, it is necessary to require that $\varepsilon^{(l)}(z) = \varepsilon_t$ and $\mu^{(l)}(z) = \mu_t$ for $z > D$, and $\varepsilon^{(l)}(z) = \varepsilon_b$ and $\mu^{(l)}(z) = \mu_b$ for $z < 0$.

In the top, we specify a plane incident wave $\{\mathbf{E}^{(i)}, \mathbf{H}^{(i)}\}$, where $\mathbf{E}$ is the electric field, $\mathbf{H}$ is the magnetic field multiplied by the free space impedance, and superscript (i) denotes the incident field. For the infinite layered medium given by $\varepsilon^{(l)}$ and $\mu^{(l)}$, the incident wave gives rise to a simple solution $\{\mathbf{E}^{(l)}, \mathbf{H}^{(l)}\}$. We call this the 1D solution in S_l. The difference $\{\mathbf{E}-\mathbf{E}^{(l)}, \mathbf{H}-\mathbf{H}^{(l)}\}$ satisfies the homogeneous Maxwell's equations in S_l, and is outgoing as $z \to \pm\infty$.

The variable z is truncated to $z_b < z < z_t$ with two perfectly matched layers (PMLs) [20, 21] ending at z_b and z_t, respectively. With this truncation, the layered medium given by $\varepsilon^{(l)}$ and $\mu^{(l)}$ supports a discrete sequence of 1D modes (i.e., the vertical modes) $\{\phi_j^{(l,p)}(z), \eta_j^{(l,p)}\}$, for $j = 1, 2, ...$, where $p \in \{e, h\}$ denotes the polarization, j is the mode index, $\phi_j^{(l,p)}(z)$ is the mode profile, and $\eta_j^{(l,p)}$ is the propagation constant. Like those in a planar waveguide, the 1D modes are either transverse electric (TE) or transverse magnetic (TM), and they satisfy

$$\frac{\mu^{(l)}}{s_z}\frac{d}{dz}\left(\frac{1}{s_z\mu^{(l)}}\frac{d\phi_j^{(l,e)}}{dz}\right) + k_0^2\varepsilon^{(l)}\mu^{(l)}\,\phi_j^{(l,e)} = [\eta_j^{(l,e)}]^2\phi_j^{(l,e)}, \tag{2}$$

$$\frac{\varepsilon^{(l)}}{s_z}\frac{d}{dz}\left(\frac{1}{s_z\varepsilon^{(l)}}\frac{d\phi_j^{(l,h)}}{dz}\right) + k_0^2\varepsilon^{(l)}\mu^{(l)}\,\phi_j^{(l,h)} = [\eta_j^{(l,h)}]^2\phi_j^{(l,h)} \tag{3}$$

for $z_b < z < z_t$, respectively, where k_0 is the free space wavenumber, $s_z = s_z(z)$ is a complex function of z related to the PMLs ($s_z \neq 1$ only in the PMLs). Equations (2) and (3) are supplemented by simple zero boundary conditions

$$\phi_j^{(l,p)}(z_t) = \phi_j^{(l,p)}(z_b) = 0. \tag{4}$$

Due to the use of PMLs and the possibly absorptive media, the propagation constant $\eta_j^{(l,p)}$ is usually complex with a positive imaginary part. Due to the process of

separation of variables in VMEM, each vertical mode is associated with a function of x and y satisfying the 2D Helmholtz equation

$$\frac{\partial^2 V_j^{(l,p)}}{\partial x^2} + \frac{\partial^2 V_j^{(l,p)}}{\partial y^2} + [\eta_j^{(l,p)}]^2 V_j^{(l,p)} = 0 \tag{5}$$

in Ω_l.

Let $\boldsymbol{\nu} = (\nu_x, \nu_y)$ and $\boldsymbol{\tau} = (-\nu_y, \nu_x)$ be a pair of orthogonal unit vectors in the xy plane, then the field in S_l (with z truncated) can be expanded in the vertical modes as follows:

$$H_z = H_z^{(l)} + \frac{1}{\mu^{(l)}} \sum_{j=1}^{\infty} [\eta_j^{(l,e)}]^2 \phi_j^{(l,e)} V_j^{(l,e)} \tag{6}$$

$$E_z = E_z^{(l)} + \frac{1}{\varepsilon^{(l)}} \sum_{j=1}^{\infty} [\eta_j^{(l,h)}]^2 \phi_j^{(l,h)} V_j^{(l,h)} \tag{7}$$

$$H_{\boldsymbol{\tau}} = H_{\boldsymbol{\tau}}^{(l)} + \frac{1}{\mu^{(l)}} \sum_{j=1}^{\infty} \frac{d\phi_j^{(l,e)}}{dz} \frac{\partial V_j^{(l,e)}}{\partial \boldsymbol{\tau}} + \mathbf{i} k_0 \sum_{j=1}^{\infty} \phi_j^{(l,h)} \frac{\partial V_j^{(l,h)}}{\partial \boldsymbol{\nu}} \tag{8}$$

$$E_{\boldsymbol{\tau}} = E_{\boldsymbol{\tau}}^{(l)} + \frac{1}{\varepsilon^{(l)}} \sum_{j=1}^{\infty} \frac{d\phi_j^{(l,h)}}{dz} \frac{\partial V_j^{(l,h)}}{\partial \boldsymbol{\tau}} - \mathbf{i} k_0 \sum_{j=1}^{\infty} \phi_j^{(l,e)} \frac{\partial V_j^{(l,e)}}{\partial \boldsymbol{\nu}}. \tag{9}$$

where $E_{\boldsymbol{\tau}}$ and $H_{\boldsymbol{\tau}}$ are the horizontal field components in the $\boldsymbol{\tau}$ direction, $\partial_{\boldsymbol{\tau}} V_j^{(l,p)}$ and $\partial_{\boldsymbol{\nu}} V_j^{(l,p)}$ are directional derivatives of $V_j^{(l,p)}$.

Let Γ be the boundary of Ω_1 (and Ω_0), and $\boldsymbol{\nu}$ be a unit normal vector of Γ, then $\partial_{\boldsymbol{\tau}}$ is the tangential derivative operator along Γ. For any function $V_j^{(l,p)}$ satisfying Eq. (5) in Ω_l, there is an operator $\Lambda_j^{(l,p)}$ (the so-called Dirichlet-to-Neumann (DtN) map), such that

$$\Lambda_j^{(l,p)} V_j^{(l,p)} = \partial_{\boldsymbol{\nu}} V_j^{(l,p)} \quad \text{on} \quad \Gamma. \tag{10}$$

Assuming $\partial_{\boldsymbol{\tau}}$ and $\Lambda_j^{(l,p)}$ can be approximated, then VMEM gives rise to a linear system

$$\mathbf{A}\boldsymbol{x} = \boldsymbol{b}, \tag{11}$$

where $\boldsymbol{x}$ is a vector for all $V_j^{(l,p)}$ on Γ. The details of $\mathbf{A}$ and $\boldsymbol{b}$ are given in [13]. Notice that we are only solving these functions on a curve (i.e. Γ). The above system is obtained by matching H_z, E_z, $H_{\boldsymbol{\tau}}$ and $E_{\boldsymbol{\tau}}$ for (x, y) on Γ and $z_b < z < z_t$. It is a 2D reformulation of the original 3D Maxwell's equations.

In the fully discretized version, the z variable is discretized by N points, the curve Γ is discretized by M points, the operators $\partial_{\boldsymbol{\tau}}$ and $\Lambda_j^{(l,p)}$ are approximated by $M \times M$ matrices, then Eq. (11) is a linear system with $4NM$ unknowns.

3. DtN maps for 2D Helmholtz equations

Clearly, a key step in VMEM is to approximate the DtN maps $\Lambda_j^{(l,p)}$ by matrices. For the case of circular cylinders, the DtN maps can be constructed from cylindrical wave expansions [13]. For elliptic cylinders, the Helmholtz equation (5) is separable in the elliptic coordinates, its solution can be expanded in Mathieu functions. In principle, the DtN map can be constructed analytically from such an expansion. However, for reasons given below, we avoid the exact Mathieu functions and use numerically calculated functions to construct the DtN maps.

Let Γ be the ellipse $(x/a)^2 + (y/b)^2 = 1$ with semi-axes a and b ($a > b$), and semifocal distance $f = \sqrt{a^2 - b^2}$. The elliptic coordinates (ϱ, ϑ) satisfy

$$x = f\cosh(\varrho)\cos(\vartheta), \quad y = f\sinh(\varrho)\sin(\vartheta) \tag{12}$$

for $\varrho \geq 0$ and $0 \leq \vartheta \leq 2\pi$, and Γ is given by

$$\varrho = \varrho_0 = \operatorname{arctanh}(b/a).$$

Since $f\cosh(\varrho_0) = a$ and $f\sinh(\varrho_0) = b$, Γ is also given by

$$x = a\cos(\vartheta), \quad y = b\sin(\vartheta). \tag{13}$$

Notice that as $b/a \to 1$, ϱ_0 tends to infinity, and ϱ does not approach the radial variable of the standard polar coordinate system. Therefore, the method developed in this section should not be used when b is equal to or close to a. On the other hand, the original VMEM [13] (with simple modifications) works when b/a is close to 1, since the cylindrical wave expansions inside and outside the ellipse converge well.

In terms of (ϱ, ϑ), Eq. (5) becomes

$$\partial_\varrho^2 V + \partial_\vartheta^2 V + 2q[\cosh(2\varrho) - \cos(2\vartheta)]V = 0, \tag{14}$$

where $q = (f\eta)^2/4$. For simplicity, we have dropped the subscript j and the superscript (l, p). Let $V = R(\varrho)S(\vartheta)$ be a solution of Eq. (14) by the method of separation of variables, then S satisfies

$$\frac{d^2 S}{d\vartheta^2} + [\lambda - 2q\cos(2\vartheta)]\, S = 0 \tag{15}$$

subject to the 2π-periodic boundary condition where λ is an eigenvalue, and R satisfies

$$\frac{d^2 R}{d\varrho^2} - [\lambda - 2q\cosh(2\varrho)]\, R = 0. \tag{16}$$

For Ω_1 (the domain inside Γ), Eq. (16) is valid for $0 < \varrho < \varrho_0$, the boundary condition is $R(0) = 0$ if the corresponding S is an odd function of ϑ with respect to $\vartheta = \pi$, i.e., $S(2\pi - \vartheta) = -S(\vartheta)$, or $R'(0) = 0$ if S is even, i.e., $S(2\pi - \vartheta) = S(\vartheta)$, where $R' = dR/d\varrho$. For the exterior domain Ω_0, Eq. (16) is valid for $\varrho > \varrho_0$, and R should be chosen to represent an outgoing wave

as $\varrho \to \infty$. The eigenvalue problem for S has a discrete sequence of eigenvalues λ_m and eigenfunctions S_m for $m = 1, 2, ...$, and the corresponding solutions of Eq. (16) are denoted as R_m. Therefore, a function V satisfying Eq. (5) in Ω_l can be expanded as

$$V(\varrho, \vartheta) = \sum_{m=1}^{\infty} c_m R_m(\varrho) S_m(\vartheta), \tag{17}$$

where c_m ($m = 1, 2, ...$) are expansion coefficients. The functions S_m ($m = 1, 2, ...$) are the angular Mathieu functions. Using the notations of Stratton [18], the even and odd angular Mathieu functions are denoted as Se_n (for $n = 0, 1, 2, ...$) and So_n (for $n = 1, 2, ...$), and they resemble $\cos(n\vartheta)$ and $\sin(n\vartheta)$, respectively. For Ω_1, the functions R_m ($m = 1, 2, ...$) are the radial Mathieu functions corresponding to Bessel functions J_m, and they are denoted as $\mathrm{Re}_n^{(1)}$ and $\mathrm{Ro}_n^{(1)}$ by Stratton [18]. For Ω_0, the functions R_m ($m = 1, 2, ...$) are the radial Mathieu functions corresponding to the Hankel functions $H_m^{(1)}$, and they are denoted as $\mathrm{Re}_n^{(3)}$ and $\mathrm{Ro}_n^{(3)}$.

From Eq. (13), we obtain the outward unit normal vector of Γ

$$\boldsymbol{\nu}(\vartheta) = \frac{1}{w(\vartheta)} \left[b\cos(\vartheta), a\sin(\vartheta) \right], \tag{18}$$

where $w(\vartheta) = (a^2 \sin^2\vartheta + b^2\cos^2\vartheta)^{1/2}$. Furthermore, the normal derivative on Γ is only related to the partial derivative with respect to ϱ, i.e.,

$$\partial_{\boldsymbol{\nu}} V = \frac{1}{w(\vartheta)} \partial_\varrho V \quad \text{at} \quad \varrho = \varrho_0. \tag{19}$$

Therefore,

$$\partial_{\boldsymbol{\nu}} V|_\Gamma = \frac{1}{w(\vartheta)} \sum_{m=1}^{\infty} c_m R_m'(\varrho_0) S_m(\vartheta), \tag{20}$$

where $R_m' = dR_m/d\varrho$. Equations (17) and (20) allow us to define the DtN operator Λ that maps V to $\partial_{\boldsymbol{\nu}} V$ on Γ.

When Γ is discretized by M points, for example, by a uniform discretization of ϑ given by $\vartheta_i = 2\pi i/M$ for $0 \le i < M$, we have two column vectors $\boldsymbol{V}$ and $\partial_{\boldsymbol{\nu}}\boldsymbol{V}$ for $V|_\Gamma$ and $\partial_{\boldsymbol{\nu}} V|_\Gamma$ at (ϱ_0, ϑ_i) for $0 \le i < M$, then we can find an $M \times M$ matrix $\boldsymbol{\Lambda}$ that approximates the DtN operator. Assuming the sums in Eqs. (17) and (20) are truncated to M terms, then

$$\boldsymbol{V} = \mathbb{S}\,\boldsymbol{h}, \quad \partial_{\boldsymbol{\nu}}\boldsymbol{V} = \mathbb{W}\mathbb{S}\mathbb{D}\,\boldsymbol{h}, \tag{21}$$

where $\mathbb{S}$ is a square matrix with columns $\boldsymbol{S}_m$ for $1 \le m \le M$, $\boldsymbol{S}_m$ is a column vector for $S_m(\vartheta_i)$ for $0 \le i < M$, $\boldsymbol{h}$ is a column vector for $c_m R_m(\varrho_0)$, $\mathbb{D}$ is a diagonal matrix with diagonal entries $R_m'(\varrho_0)/R_m(\varrho_0)$ for $1 \le m \le M$, and $\mathbb{W}$ is a diagonal matrix with diagonal entries $1/w(\vartheta_i)$ for $0 \le i < M$. Eliminating the vector $\boldsymbol{h}$, we obtain $\partial_{\boldsymbol{\nu}}\boldsymbol{V} = \boldsymbol{\Lambda}\boldsymbol{V}$, where

$$\boldsymbol{\Lambda} = \mathbb{W}\mathbb{S}\mathbb{D}\mathbb{S}^{-1}. \tag{22}$$

The above formula for the DtN map works in principle, but for a complex η with a large imaginary part, the angular Mathieu functions $S_m(\vartheta)$ could have very different magnitudes at different values of ϑ. In that case, the matrix $\mathbb{S}$ is nearly singular, and it becomes difficult to calculate $\boldsymbol{\Lambda}$ accurately using Eq. (22), since $\mathbb{S}^{-1}$ is involved.

To overcome this difficulty, we replace the analytic Mathieu functions by numerically calculated functions. For Eq. (15), we discretize ϑ by M points as above and approximate the derivatives with respect to ϑ by Fourier differentiation matrices [22]. Therefore, the eigenvalue problem for S is approximated by an $M \times M$ matrix eigenvalue problem. Among the M numerical eigenvalues, some, but not all, are good approximations to the exact eigenvalues. In our experience, the matrix of all M numerical eigenvectors is better conditioned than the original matrix $\mathbb{S}$ obtained by sampling the exact angular Mathieu functions, and it is used to replace $\mathbb{S}$ in Eq. (22).

For each numerical eigenvalue λ_m, we solve a two-point boundary value problem (BVP) for R_m satisfying Eq. (16). Since λ_m is not an exact eigenvalue of Eq. (15), the solution of this BVP is not identical to a radial Mathieu function. As mentioned above, the BVP is for $0 < \varrho < \varrho_0$ or $\varrho > \varrho_0$ corresponding to domain Ω_1 or Ω_0, respectively. The boundary condition at ϱ_0 is simply assumed to be $R_m(\varrho_0) = 1$. For the case of Ω_1, the boundary condition at $\varrho = 0$ is either $R_m(0) = 0$ or $R_m'(0) = 0$ depending on whether $S_m(\vartheta)$ is an odd or even function of ϑ with respect to $\vartheta = \pi$. We use the Chebyshev collocation method [22] to solve the two-point BVP for R_m and find $R_m'(\varrho_0)$, then construct the matrix $\mathbb{D}$.

For the case of Ω_0, the BVP problem is considered for $\varrho > \varrho_0$, and the solution could be highly oscillatory (in ϱ) as $\varrho \to \infty$. To avoid this, we let $\varsigma = \exp(\varrho)$, then Eq. (16) becomes

$$\frac{d^2R}{d\varsigma^2} + \frac{1}{\varsigma}\frac{dR}{d\varsigma} + \left(q - \frac{\lambda}{\varsigma^2} + \frac{q}{\varsigma^4} \right) R = 0 \tag{23}$$

for $\varsigma > \varsigma_0 = \exp(\varrho_0)$. Since R represents an outgoing wave as $\varsigma \to \infty$, it should satisfy the following Summerfeld radiation condition

$$\lim_{\varsigma\to\infty} \sqrt{\varsigma} \left(\frac{dR}{d\varsigma} - \frac{\mathbf{i} f\eta}{2} R \right) = 0. \tag{24}$$

Notice that $f\eta/2 = \sqrt{q}$. For practical computation, it is more effective to truncate ς by a PML [20, 21]. More precisely, we introduce a complex function of ς denoted as $\hat{\varsigma}$, and replace ς in Eq. (23) by $\hat{\varsigma}$. It leads to

$$\frac{1}{s_\varsigma}\frac{d}{d\varsigma}\left(\frac{1}{s_\varsigma}\frac{dR}{d\varsigma} \right) + \frac{1}{\hat{\varsigma} s_\varsigma}\frac{dR}{d\varsigma} + \left(q - \frac{\lambda}{\hat{\varsigma}^2} + \frac{q}{\hat{\varsigma}^4} \right) R = 0, \tag{25}$$

where $s_\varsigma = d\hat{\varsigma}/d\varsigma$. The variable ς is truncated to $\varsigma_0 < \varsigma < \varsigma_2$, and the actual PML is given by $\varsigma_1 < \varsigma < \varsigma_2$

where $\varsigma_1 > \varsigma_0$. This implies that $\hat{\varsigma} = \varsigma$ and $s_\varsigma = 1$ for $\varsigma_0 < \varsigma < \varsigma_1$. Equation (25) is supplemented with the boundary conditions

$$R(\varsigma_0) = 1, \quad R(\varsigma_2) = 0. \tag{26}$$

We solve BVP (25) and (26) by a Chebyshev collocation method [22].

After a matrix approximation of the DtN operator Λ is obtained, we can validate the result and check its accuracy using exact solutions of the Helmholtz equation. For Ω_1, the exact solutions can be plane waves or cylindrical waves. For Ω_0, we use outgoing cylindrical waves radiating from any point in Ω_1. If V is an exact solution, we can evaluate V on Γ, find ΛV and compare it with the exact $\partial_{\boldsymbol{\nu}} V$ on Γ.

The DtN operators can be efficiently calculated, since they are solved from independent 2D problems which are further reduced to simple 1D two-point BVPs. Overall, the time spent on computing the $4N$ DtN operators is negligible compared with the time for solving the final linear system (11).

For setting up the linear system (11), a matrix approximating the tangential derivative operator along Γ is needed. Since $\partial_{\boldsymbol{\tau}} = [w(\vartheta)]^{-1}\partial_\vartheta$, this matrix can be obtained from the Fourier differentiation matrix that approximates ∂_ϑ [22]. After $V_j^{(l,p)}$ on Γ are solved, we use the fully numerical version of (17) to construct the electromagnetic field in each region.

4. Elliptic apertures in a metallic film

In this section, we follow Zakharian *et al.* [19], consider the transmission of light through an elliptic hole in a silver film of thickness $D = 0.124\,\mu$m, where the semi-axes of the elliptic hole are $a = 0.4\,\mu$m and $b = 0.05\,\mu$m, respectively. The medium below and above the film, and inside the hole, is air, thus $\varepsilon_t = \varepsilon_b = 1$. The structure is non-magnetic, thus $\mu = 1$ everywhere. The problem is considered for normal incident plane waves with a free space wavelength of $1\,\mu$m. The refractive index of silver is assumed to be $n = 0.226 + 6.99\mathbf{i}$.

Since the aspect ratio of the ellipse is quite large ($a/b = 8$), the elliptic hole is quite similar to a slit parallel to the x axis. If the incident wave has an electric field parallel to the x axis, transmission is very low. In Fig. 2, we show the z components of the electromagnetic field at 19.1 nm below the metal film for an incident wave with $E_x^{(i)} = \exp(-\mathbf{i}k_0 z)$, $E_y^{(i)} = E_z^{(i)} = 0$. In contrast, high transmission is possible when the electric field of the incident wave is parallel to the y axis. In Fig. 3, we show E_z and H_z at the same horizontal plane for an incident wave with $E_y^{(i)} = \exp(-\mathbf{i}k_0 z)$ and $E_x^{(i)} = E_z^{(i)} = 0$. Notice that the field components shown in Fig. 3 have much larger magnitudes compared with those in Fig. 2.

Zakharian *et al.* [19] also considered silver films with thickness $D = 0.186\,\mu$m and $0.248\,\mu$m for the same elliptic hole and same incident waves. Using the method developed in previous section, we analyze the problem for D up to $1\,\mu$m. The results are shown in Fig. 4, where

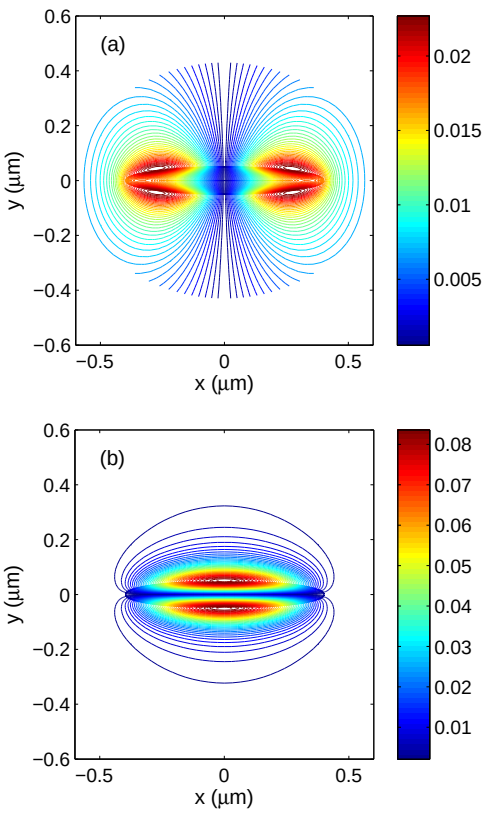

Fig. 2. Contour plots of $|E_z|$ and $|H_z|$ at 19.1 nm below a silver film for an incident wave with an electric field parallel to the x axis: (a) plot of $|E_z|$; (b) plot of $|H_z|$.

the normalized transmission coefficient T is defined as the ratio of total transmitted power (or the additional transmitted power if the film without the hole is not opaque) and the power of incident wave impinging on the elliptic aperture. Notice that T is very small if the incident electric field is parallel to the x axis, and much larger when the incident electric field is parallel to the y axis. In the latter case, T varies with D and can be larger than 3 for some values of D. This is consistent with other studies on extraordinary optical transmissions [23, 24].

For a circular hole in a metallic film, previous studies indicate that transmission may be enhanced by filling the hole with a dielectric material [13, 25, 26]. We consider the silver film with thickness $D = 0.124\,\mu$m again, and fill the elliptic hole with a dielectric material of refractive index n_c. It turns out that if the incident electric field is parallel to the x axis, transmission remains very low. On the other hand, if the incident electric field is parallel to the y axis, transmission could be enhanced if n_c is chosen correctly. In Fig. 5, we show the normalized transmission coefficient T as a function of n_c. A maximum of T is obtained for n_c around 2.9.

The above numerical results are obtained using $M = 20$ points for discretizing the ellipse and $N = 177$ for discretizing the vertical axis. For $D = 0.124\,\mu$m, the

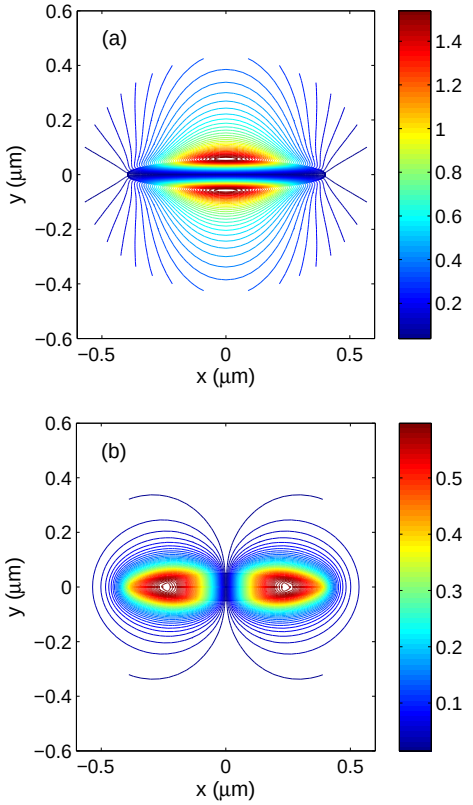

Fig. 3. Contour plots of $|E_z|$ and $|H_z|$ at $19.1nm$ below a silver film for an incident wave with an electric field parallel to the y axis: (a) plot of $|E_z|$; (b) plot of $|H_z|$.

z axis is truncated to (z_b, z_t) where $z_b = -0.2\,\mu$m and $z_t = D + 0.2\,\mu$m. A Chebyshev collocation method is used to solve the vertical modes satisfying Eqs. (2), (3) and (4). The interval (z_b, z_t) is discretized separately in three subintervals $(z_b, 0)$, $(0, D)$ and (D, z_t) using 59 interior Chebyshev points in each subinterval. In the top and bottom layers, PMLs are introduced so that the function s_z is given by

$$s_z(z) = \begin{cases} 1 + S_t[(z - \tilde{z}_t)/(z_t - \tilde{z}_t)]^3, & z > \tilde{z}_t, \\ 1, & \tilde{z}_b \le z \le \tilde{z}_t, \\ 1 + S_b[(z - \tilde{z}_b)/(z_b - \tilde{z}_b)]^3, & z < \tilde{z}_b, \end{cases}$$

where $S_t = S_b = 7 + 15\mathbf{i}$, and both intervals $(\tilde{z}_t, z_t)$ and $(z_b, \tilde{z}_b)$ contain 47 Chebyshev points.

5. Elliptic cylinders on a substrate

In recent years, metallic nanoparticles have been intensively studied due to their many applications in nanotechnology [27]. In this section, we use VMEM to analyze the scattering of plane incident waves by gold elliptic cylinders on a substrate. First, we consider elliptic cylinders with height $D = 30\,$nm and aspect ratio $a/b = 1.55$, where a and b are the semi-axes (along the x and y axes respectively) of the elliptic cross section. The cylinder is placed on a dielectric substrate with a

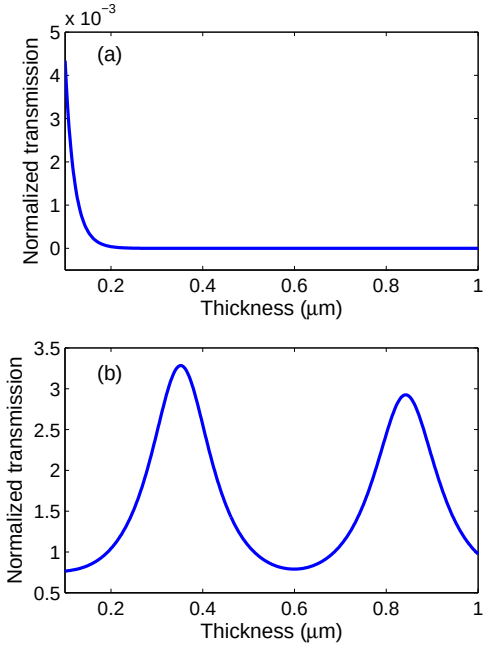

Fig. 4. Normalized transmission coefficient T versus thickness D for a silver film with an elliptical air hole. (a) $\mathbf{E}^{(i)}$ is parallel to the x axis; (b) $\mathbf{E}^{(i)}$ is parallel to the y axis.

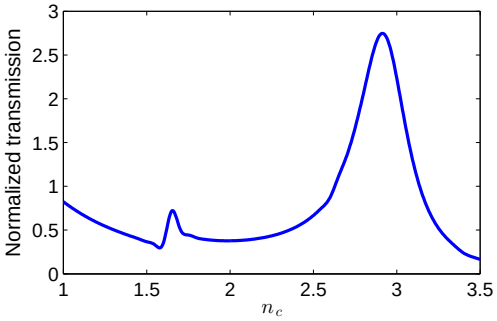

Fig. 5. Normalized transmission T for a silver film with thickness $D = 124$ nm and an elliptical hole filled with a dielectric medium of refractive index n_c.

refractive index $n = 1.5$. The medium surrounding the cylinder and above the substrate is air. The cylinder-substrate interface is in the xy plane. As in [28], we consider a number of elliptic cylinders of different size for a normal incident wave with an electric field in the y direction. The refractive index of gold is taken from the work of Johnson and Christy [29]. In Fig. 6, we show the normalized scattering cross section (defined as the total outgoing power of the scattering field, divided by the area of the elliptic cross section and the intensity of the incident wave) for short-axis length $2b = 84\,$nm, 91 nm, 96 nm, 102 nm and 104 nm. The scattering field is the difference between the total field and the 1D solution $\{\mathbf{E}^{(0)}, \mathbf{H}^{(0)}\}$, i.e., the solution obtained for a structure with only the substrate and air. From Fig. 6, it can be seen that similar to the experimental results of Su *et al.*

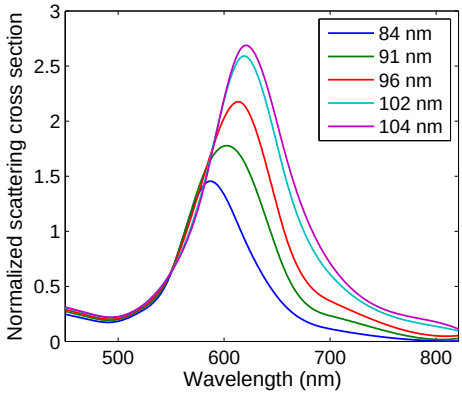

Fig. 6. Normalized scattering cross section of gold elliptic cylinders with different short-axis length ($2b$) and fixed aspect ratio $a/b = 1.55$.

[28], the resonant wavelength increases as the size of the cylinder is increased.

Next, we consider a gold elliptic cylinder with semi-axes $a = 66\,\text{nm}$, $b = 47.5\,\text{nm}$ (along the x and y directions, respectively), and height $D = 109\,\text{nm}$. It is placed on the same substrate with refractive index $n = 1.5$. The surrounding medium above the substrate is also air. As in [30], we consider two normal incident plane waves with the electric field parallel to the x and y axes, respectively. In Fig. 7, we show the normalized scattering

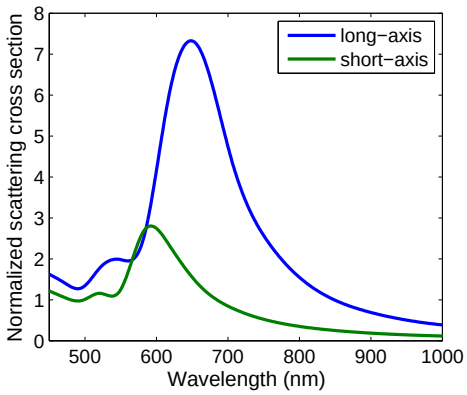

Fig. 7. Normalized scattering cross section of a gold elliptical cylinder with semi-axes $a = 66\,\text{nm}$, $b = 47.5\,\text{nm}$, and height $D = 109\,\text{nm}$, and for incident plane waves with the electric field along the long and short axes of the ellipse, respectively.

cross section for these two incident waves. For these two cases, the scattered power peaks at 649 nm and 592 nm, respectively.

For the examples in this section, we discretize z by $N = 165$ points and discretize the ellipse Γ by $M = 24$ points.

6. Conclusion

In this paper, we developed a frequency domain numerical method (VMEM) for analyzing elliptic cylindrical objects in a layered background. VMEM gives a 2D formulation for 3D problems involving structures that are layered in a cylindrical region and the surrounding media. Unlike the analytic approach used in the earlier work for circular cylindrical objects [13], we numerically solve the ordinary differential equations derived by separation of variables in the elliptic coordinates, to calculate the DtN maps for 2D Helmholtz equations (with complex coefficients) inside or outside the ellipse. The method is applied to analyze the transmission of light through an elliptic aperture in a metallic film, and the scattering of light by metallic cylinders with an elliptic cross section.

In our implementation, highly accurate Chebyshev and Fourier pseudospectral methods [22] are used for computing the vertical modes and the DtN maps, but the overall convergence rate of the method is still limited due to the field singularities along the edges of the cylinders. VMEM is currently being extended to more general structures involving multiple cylindrical objects with arbitrary cross-sections. It is also highly desirable to develop a strategy for choosing computational parameters (including those for PMLs) to reach a given level of accuracy. The computational complexity of VMEM is dominated by the step for solving the final linear system (11). We hope that a more efficient solver for Eq. (11) can be developed based on iterative methods with a suitable preconditioner.

Acknowledgment

This work was partially supported by the Research Grants Council of Hong Kong Special Administrative Region, China, under Project CityU 11301914.

References

[1] A. Taflove and S. C. Hagness, *Computational Electrodynamics: the Finite-Difference Time-Domain Method*, 2nd ed. (Artech House, 2000).

[2] J. M. Jin, *The Finite Element Method in Electromagnetics*, 2nd ed. (John Wiley & Sons, 2002).

[3] P. Monk, *Finite Element Methods for Maxwell's Equations* (Oxford Univ. Press, 2003).

[4] W. C. Chew, M. S. Tong, and B. Hu, *Integral Equation Methods for Electromagnetic and Elastic Waves* (London: Morgan & Claypool, 2008).

[5] J.-C. Nédélec, *Acoustic and Electromagnetic Equations: Integral Representations for Harmonic Problems* (Springer-Verlag, 2001).

[6] L. Li, "New formulation of the Fourier modal method for crossed surface-relief gratings," J. Opt. Soc. Am. A **14**, 2758-2767 (1997).

[7] E. Silberstein, P. Lalanne, J.-P. Hugonin, and Q. Cao, "Use of grating theories in integrated optics," J. Opt. Soc. Am. A **18**, 2865-2875 (2001).

[8] G. Granet and J. P. Plumey, "Parametric formulation of the Fourier modal method for crossed surface-relief gratings," J. Opt. A **4**, S145-S149 (2002).

[9] M. Hammer, "Hybrid analytical/numerical coupled-mode modeling of guided wave devices," J. Lightw. Technol. **25**(9), 2287-2298 (2007).

[10] J. Mu and W. P. Huang, "Simulation of three-dimensional waveguide discontinuities by a full-vector mode-matching method based on finite-difference schemes," Opt. Express **16**, 18152-18163 (2008).

[11] R. Wang, L. Han, J. Mu, and W. P. Huang, "Simulation of waveguide crossings and corners with complex mode-matching method," J. Lightw. Technol. **30**, 1795-1801 (2012).

[12] V. Liu and S. Fan, "S^4: A free electromagnetic solver for layered periodic structures," Computer Physics Communications **183**, 2233-2244 (2012).

[13] X. Lu, H. Shi, and Y. Y. Lu, "Vertical mode expansion method for transmission of light through a single circular hole in a slab," J. Opt. Soc. Am. A **31**, 293-300 (2014).

[14] S. Boscolo and M. Midrio, "Three-dimensional multiple-scattering technique for the analysis of photonic-crystal slabs," J. Lightw. Technol. **22**, 2778-2786 (2004).

[15] L. Yuan and Y. Y. Lu, "Dirichlet-to-Neumann map method for analyzing hole arrays in a slab," J. Opt. Soc. Am. B **27**, 2568-2579 (2010).

[16] L. Yuan and Y. Y. Lu, "An efficient numerical method for analyzing photonic crystal slab waveguides," J. Opt. Soc. Am. B **28**, 2265-2270 (2011).

[17] M. Abramowitz and I. Stegun, *Handbook of Mathematical Functions* (Dover, New York, 1964), Chap. 20.

[18] J. A. Stratton, *Electromagnetic Theory* (McGraw-Hill, New York, 1941), Chap. 6.

[19] A. R. Zakharian, M. Mansuripur, and J. V. Moloney, "Transmission of light through small elliptical apertures," Opt. Express **12**, 2631-2648 (2004).

[20] J. P. Berenger, "A perfectly matched layer for the absorption of electromagnetic waves," J. Comput. Phys. **114**, 185-200 (1994).

[21] W. C. Chew and W. H. Weedon, "A 3D perfectly matched medium from modified Maxwells equations with stretched coordinates," Microwave and Optical Technology Letters **7**, 599-604 (1994).

[22] L. N. Trefethen, *Spectral Methods in MATLAB*, (Society for Industrial and Applied Mathematics, 2000).

[23] T. W. Ebbesen, H. J. Lezec, G. F. Ghaemi, T. Thio, and P. A. Wolff, "Extraordinary optical transmission through sub-wavelength hole arrays," Nature **391**, 667-669 (1998).

[24] F. J. García-Vidal, L. Martin-Moreno, T. W. Ebbesen, and L. Kuipers, "Light passing through subwavelength apertures," Rev. Mod. Phys. **82**, 729–787 (2010).

[25] J. Olkkonen, K. Kataja, and D. Howe, "Light transmission through a high index dielectric-filled subwavelength hole in a metal film," Opt. Express **13**, 6980-6989 (2005).

[26] H. Xu, P. Zhu, H. G. Craighead, and W. W. Webb, "Resonantly enhanced transmission of light through subwavelength apertures with dielectric filling," Opt. Commun. **282**, 1467-1471 (2009).

[27] S. A. Maier, *Plasmonics: Fundamentals and Applications* (Springer, 2007).

[28] K. Su, Q. Wei, X. Zhang, J. Mock, D. Smith, and S. Schultz, "Interparticle coupling effects on plasmon resonances of nanogold particles," Nano. Lett. **3**, 1087-1090 (2003).

[29] P. Johnson and R. Christy, "Optical constants of the noble metals," Phys. Rev. B **6**, 4370-4379 (1972).

[30] R. Giannini, C. Hafner, and J. Löffler, "Axis-selective excitation of gold nanoparticle resonances," J. Opt. Soc. Am. B **31**, 2621-2627 (2014).